

Article

Interaction of Carbon Nanotubes, Capped Carbon Nanotubes, CNT₂₋₅, C₆₀, C₇₀, HO-C₆₀, [C₆₀]₂, and [C₆₀]₃ Fullerenes with Virulence Factors of Gram-Negative and Gram-Positive Bacteria: Potential Applications for 3D-Printed Scaffolds

Mehran Alavi ¹, Morahem Ashengroph ^{1,*} and M. R. Mozafari ²

¹ Department of Biological Science, Faculty of Science, University of Kurdistan, Sanandaj 6617715175, Iran; mehranbio83@gmail.com or m.alavi@uok.ac.ir

² Australasian Nanoscience and Nanotechnology Initiative (ANNI), 8031 Monash University LPO, Clayton, VIC 3168, Australia; dr.m.r.mozafari@gmail.com

* Correspondence: m.ashengroph@uok.ac.ir

Abstract: The antimicrobial application of carbon nanomaterials, such as carbon nanotubes (CNTs), capped CNTs, CNT₂₋₅, C₆₀, C₇₀, HO-C₆₀, [C₆₀]₂, and [C₆₀]₃ fullerenes, is increasing, owing to their low cytotoxicity properties compared to other nanomaterials such as metallic nanoparticles. Enhanced mechanical properties and antibacterial activity can be caused by the incorporation of CNTs in 3-dimensional (3D) printed nanocomposites (NCs). The interruption of the bacterial membrane resulting from the cylindrical shape and high aspect ratio properties has been found to be the most prominent antibacterial mechanism of CNTs. However, the unraveling interaction of CNTs, capped CNTs, CNT₂₋₅, C₆₀, C₇₀, HO-C₆₀, [C₆₀]₂, and [C₆₀]₃ fullerenes with virulence factors of the main bacterial pathogenesis has not yet been understood. Therefore, in the present study, interactions of these carbon-based nanomaterials with the eight virulence factors, including protein kinase A and (ESX)-secreted protein B of *Mycobacterium tuberculosis*, pseudomonas elastase and exotoxin A of *Pseudomonas aeruginosa*, alpha-hemolysin and penicillin-binding protein 2a of *Staphylococcus aureus*, and shiga toxin 2a and heat-labile enterotoxin of *Escherichia coli*, were evaluated with the molecular docking method of AutoDock Vina. This study disclosed that the binding affinity was highest for CNT₂₋₅ and [C₆₀]₃ toward alpha-hemolysin, with binding energies of −32.7 and −26.6 kcal/mol, respectively. The stability of the CNT₂₋₅-alpha-hemolysin complex at different times was obtained according to the normal mode analysis of *ElNémo* and *iMOD* servers.

Keywords: 3D-printed scaffolds; carbon nanotube; capped carbon nanotube; protein kinase A; pseudomonas elastase; exotoxin A; alpha-hemolysin; shiga toxin 2a



Citation: Alavi, M.; Ashengroph, M.; Mozafari, M.R. Interaction of Carbon Nanotubes, Capped Carbon Nanotubes, CNT₂₋₅, C₆₀, C₇₀, HO-C₆₀, [C₆₀]₂, and [C₆₀]₃ Fullerenes with Virulence Factors of Gram-Negative and Gram-Positive Bacteria: Potential Applications for 3D-Printed Scaffolds. *Inorganics* **2024**, *12*, 77. <https://doi.org/10.3390/inorganics12030077>

Academic Editor: Isabel Correia

Received: 16 January 2024

Revised: 21 February 2024

Accepted: 26 February 2024

Published: 1 March 2024



Copyright: © 2024 by the authors. Licensee MDPI, Basel, Switzerland. This article is an open access article distributed under the terms and conditions of the Creative Commons Attribution (CC BY) license (<https://creativecommons.org/licenses/by/4.0/>).

1. Introduction

Emerging antibiotic resistance in various bacterial strains is a great therapy challenge, specifically in the case of health-threatening infections such as septicemia and chronic infectious wounds [1–3]. Therefore, there is an urgent need to find new, effective, biocompatible antibacterial agents. Nanomaterials, particularly carbon nanotubes (CNTs) and fullerenes, can be regarded as suitable nanomaterials for hindering bacterial infections because of their unique physicochemical properties at the nanoscale [4]. Moreover, these nanomaterials with large specific surface areas and aspect ratios have been used to upgrade various safe scaffolds for tissue engineering [5]. Providing biocompatible and biodegradable scaffolds for tissue engineering is critical to improving the attachment and migration of cells and delivering and retaining cells and biological macromolecules [6]. Based on material sources, there are four classes of scaffold materials, including nano-scaffold materials, composite scaffold materials, synthetic biodegradable scaffold materials,

and natural biological scaffold materials [7]. In this way, various novel techniques have been presented for the formation of scaffolds suitable for bone regeneration, cartilage, and artificial skin [8–10]. Three-dimensional (3D) printing technology based on computer-aided design (CAD) technology software and computed tomography (CT) is a promising technique specifically for personalized therapies [11]. In regenerative medicine, 3D printing techniques may be utilized to fabricate implants and scaffolds, including calvarial bone grafts and tracheobronchomalacia [12]. In addition, this technology had a significant impact on aerospace and mechanical manufacturing [13]. Three-dimensional printing techniques are classified according to printing methods and the types of materials. In a fused deposition modeling (FDM)-type printer such as the common 3D printing method, the melted filaments of a wide range of biocompatible and biodegradable polymers, such as polylactic acid (PLA) [14] and poly(ϵ -caprolactone) (PCL)/thermoplastic polysaccharide, can be extruded directly from the nozzle and deposited on the substrate layer-by-layer as the thin film [15]. Four main steps for 3D printing include digital model design, digital slicing, G-code conversion, and manufacturing the 3D model [16]. As the main advantage, toxic organic solvents are not needed to dissolve the polymeric filaments for this type of printing [11]. Two major limitations of FDM are low-resolution printing and the requirement of a high temperature during the melt-extrusion stage, which can change the physicochemical properties of precursors [17]. The application of nanomaterials (NMs) such as metal nanoparticles (silver, zinc oxide, and copper oxide) and CNTs concomitant with thermoplastic polymers for 3D printing has provided novel physicochemical and therapeutic properties [18]. CNTs are produced from carbon atoms with a cylindrical structure (single-wall carbon nanotubes (SWCNTs) and multi-wall carbon nanotubes (MWCNTs)) intermediate between flat graphene and fullerene cages [19]. SWCNTs can be found in chiral, armchair, and zigzag forms. The main configurations of CNTs, involving zigzag ($\theta = 0^\circ$) and armchair ($\theta = 30^\circ$) forms, are made according to the geometry of the carbon bonds around the circumference of the tube [20]. Moreover, the ends of CNTs can be enclosed in fullerene-like cages as capped CNTs [21]. Tough hydrogels incorporated with carbon nanotubes as biohybrid scaffolds accelerated the regeneration of calvarial defect healing in bone regeneration [22]. Additionally, sodium alginate, gelatin, and CNTs were applied to construct cylindrical scaffolds with improved mechanical properties and low cytotoxicity [23]. Moreover, SWNTs illustrated significant membrane damage and loss of viability against *E. coli* after 60 min of incubation [24,25]. The main antibacterial mechanisms for CNTs can result from their cylindrical shape and high aspect ratio, followed by their penetration into cell membranes [26,27]. In the case of fullerenes such as C_{60} and C_{70} , the main antibacterial mechanisms can be reactive oxygen species (ROS) production, specifically 1O_2 , DNA damage, cell membrane disruption, and protein denaturation [28]. As a critical point, the interaction of CNTs, capped CNTs, CNT_{2-5} , C_{60} , C_{70} , HO- C_{60} , $[C_{60}]_2$, and $[C_{60}]_3$ with biological macromolecules and virulence factors of Gram-negative and Gram-positive bacteria has not yet been comprehensively recognized [29–31]. The antibacterial activity of these carbonic nanomaterials has not been comprehensively investigated against the specific proteins of both Gram-negative and Gram-positive bacteria. In this regard, an in silico study can help address this issue by selecting carbonic nanomaterials with effective antibacterial potential [32]. There are well-known virulence factors for four main human pathogenic bacteria, including *Mycobacterium tuberculosis*, *Pseudomonas aeruginosa*, *Staphylococcus aureus*, and *Escherichia coli*, which can be employed to evaluate the antibacterial effects of CNTs, capped CNTs, CNT_{2-5} , C_{60} , C_{70} , HO- C_{60} , $[C_{60}]_2$, and $[C_{60}]_3$.

Direct cytopathic effects, hindering protein synthesis and interfering with cellular immune functions, can be caused by exotoxin A, the most toxic virulence factor of *P. aeruginosa* [33]. Tissue damage during infection in human cells has been found for pseudomonas elastase as a major virulence factor of *P. aeruginosa* [34]. In the case of *S. aureus*, alpha-hemolysin, as a pore-forming toxin, can disrupt the host cell plasma membrane [35]. Penicillin-binding protein 2a of methicillin-resistant *S. aureus* (MRSA) leads to the resistance of these bacteria to various antibiotics [36]. *M. tuberculosis* mediates cell growth and

survival in vitro and in vivo by protein kinase A (PknA) [37]. In addition, mycobacterial ESX-secreted protein B contributes to the survival of *M. tuberculosis* against the immune system via suppressing interferon- γ -induced autophagy in macrophages and damaging the phagosome membrane [38]. For *E. coli*, heat-labile enterotoxin causes watery diarrhea in enterotoxigenic *E. coli* infection, and shiga toxin related to *E. coli* O157:H7 leads to bloody diarrhea and hemolytic uremic syndrome [39,40]. In this way, we have tried to reveal the interaction of CNTs and capped CNTs with the main virulence factors, including *Escherichia coli* (heat-labile enterotoxin and shiga toxin), *Mycobacterium tuberculosis* (ESX-secreted protein B and the serine/threonine protein kinase), *P. aeruginosa* (pseudomonas elastase and exotoxin A), and *Staphylococcus aureus* (alpha-hemolysin and protein 2a) via molecular docking.

2. Results

2.1. Molecular Docking

In this study, the interaction of the carbonic NMs, including CNTs, capped CNTs, CNT₂₋₅, C₆₀, C₇₀, HO-C₆₀, [C₆₀]₂, and [C₆₀]₃ with the major virulence factors of shiga toxin 2a, alpha-hemolysin, protein kinase A, elastase, exotoxin A, heat-labile enterotoxin, penicillin-binding protein 2a, and ESX-secreted protein B, is explored. Generally, docking scores obtained from AutoDock Vina disclosed that CNTs compared to fullerenes had more affinity for bacterial virulence factors (Tables 1–3). This may result from the morphology of CNTs, with their tubular shape compared with the spherical shape of fullerenes. In the case of three types of CNTs, lower and higher energies of binding with values of -32.7 and -11.9 kcal/mol were found for 7AHL and 1EZM receptors, respectively (Table 1). CNT₂₋₅ illustrated the highest binding affinity toward 7AHL with a binding energy of -32.7 kcal/mol (Figure 1a). For this interaction, the interacting amino acids were ASN123, THR125, ASP127, LEU135, LYS147, ASN121, MET113, and GLU111 (Table 1). For the CNT and 7AHL receptors, there were interacting amino acids, including THR125, LYS131, LEU135, ASN121, ASN123, LEU135, ASN121, ASN123, LEU135, ASN121, THR125, GLY126, and ASP127. Among all receptors, the lowest and highest binding affinities were found for CNTs against 1TII and 1MWT with binding energy values of 97.4 and -20.1 kcal/mol (Table 1). Common interacting amino acids for CNT-1MWT and capped CNT-1MWT complexes were ASN146, LYS148, GLU170, GLN199, GLN200, GLN203, TRP205, PRO213, THR238, PRO258, ILE259, ASP274, ASP275, and ILE309. Based on different interacting amino acids for these ligands, asparagine (ASN236 and ASN260: aliphatic amino acids) and serine (SER261: a polar amino acid) were found specifically for the CNT-1MWT docking complex (Table 1). Moreover, the donor/acceptor surface for the best pose in terms of the H-bond interaction of CNT-1MWT was indicated on the solid surface by X, Y, and Z sizes of 5.67, 24.63, and -22.64 Å, respectively. CNT₂₋₅ could not find any conformations completely within the search space of the 1TII receptor (Table 1).

Table 1. Binding affinities (kcal/mol) and interacting residues contributing to interactions of CNTs, capped CNTs, and CNT₂₋₅ with 7D6Q, 7AHL, 4OW8, 1IKQ, and 1EZM receptors (R: receptor; IAA: interacting amino acid; and (-): without docking).

R	CNT	IAA	Capped CNT	IAA	CNT ₂₋₅	IAA
7D6Q	-14.4	ASP94, ASP111, SER113, PRO258, ASP70, LYS5, GLY6, LYS7, GLU9, ASP24	-16.1	ASP94, ASP111, SER113, PRO258, GLN261, ASN69, ASP70, LYS5, LYS7, GLU9, ASP24	-19.8	GLU177, GLN180, VAL188, TYR189, THR190, ASN226, ASP70, LYS5, GLY6, LYS7, ASP24

Table 1. Cont.

R	CNT	IAA	Capped CNT	IAA	CNT ₂₋₅	IAA
1TII	97.4	GLU22, THR24, LYS25, SER42, SER74, GLY75, MET76, ARG77, GLY1, ALA98, ARG15, ARG16, GLY18, ALA28, TYR29, GLU30, ARG31, LEU119, ARG141, ASP142	79	GLU22, THR24, LYS25, SER42, SER74, GLY75, MET76, ARG77, GLY1, ALA98, ARG15, ARG16, GLY18, ALA28, GLU30, ARG31, LEU119, ARG141, ASP142	-	-
7AHL	-19.6	THR125, LYS131, LEU135, ASN121, ASN123, LEU135, ASN121, THR125, GLY126, ASP127	-18.8	LEU116, TYR118, VAL140, TYR112, HIS144, TRP179, PRO181, TYR182, SER186, TRP187, ASN188, PRO189, GLN194, ASN178, TRP179	-32.7	ASN123, THR125, ASP127, LEU135, LYS147, ASN121, MET113, GLU111
1MWT	-20.1	ASN146, LYS148, GLU170, GLN199, GLN200, GLN203, TRP205, PRO213, ASN236, THR238, PRO258, ILE259, ASN260, SER261, ASP274, ASP275, ILE309	-19.6	ASN146, LYS148, GLU170, GLN199, GLN200, GLN203, TRP205, PRO213, THR238, PRO258, ILE259, ASP274, ASP275, ARG298, ILE309	-19.4	ASP82, LYS84, GLN98, ASN111, TYR169, SER225, LYS229, HIS232, LYS331, LYS334, GLU658
4OW8	-13.0	ARG112, SER212, LYS214, PRO216, ALA218, LYS228, PRO235, PRO238, ASP240	-12.6	ARG112, SER212, LYS214, PRO216, ALA218, LYS228, PRO235, PRO238, ASP240	-13.5	LYS108, THR110, GLY111, ARG112, SER212, GLY213, LYS214, ASP240
7P13	-16.6	ALA186, ASP189, GLN190, ASN274, GLN190, GLN193, HIS197, PRO276, LYS277, PRO279, PRO280	-16.3	ALA186, ASP189, GLN190, GLN190, GLN193, HIS197, PRO276, LYS277, PRO279, PRO280	-26.3	GLU263, ASN266, LYS267, HIS197, TYR211, GLU271, ASN274, PRO276, ALA186, ASP189, GLN190, GLN193
1IKQ	-12.9	ARG213, ASN215, ASP218, GLU221, ASP403, GLU431	-13.2	ARG213, ASN215, ASP218, GLU221, and GLU431	-18.8	HIS128, ASP238, LYS240, ARG352, ALA464, ILE465, LEU535, PRO536, ARG538
1EZM	-11.9	ASN112, TYR114, TRP115, ASP116, ASP136, GLU148, TYR155, GLU172, GLU175, ASP183, LEU185	-12.3	ASN112, TRP115, ASP116, ASP136, GLU148, TYR155, GLU172, GLU175, ASP183, LEU185	-12.8	ALA1, ILE25, VAL26, ASN27, ASP28, ASP34, GLY35

Table 2. Binding affinities (kcal/mol) and interacting residues contributing to interaction of C₆₀ and C₇₀ with 7D6Q, 7AHL, 4OW8, 1IKQ, and 1EZM receptors (R: receptor and IAA: interacting amino acid).

R	C ₆₀	IAA	C ₇₀	IAA
7D6Q	-10.1	LYS270, ASN272, ASN273, LYS7, GLY46, ASN69, ASP70	-10.0	GLN118, ARG119, LEU123, GLU124, LYS5, GLN66, ASP70, GLU9, LYS22

Table 2. Cont.

R	C ₆₀	IAA	C ₇₀	IAA
1TII	−4.9	THR24, LYS25, SER42, GLY1, ALA98, ARG141	−2.5	GLU22, THR24, LYS25, SER42, GLY1, ALA98 ARG15, ARG141, ASP142
7AHL	−12.8	ARG104, ASN105, SER106, ILE107, TYR102, PRO103, THR155, PHE224, SER225, ASP227	−13.6	ARG104, ASN105, SER106, ILE107, TYR102, PRO103, THR155, PHE224, SER225, ASP227
1MWT	−10.4	TYR255, ASN260 PHE371, GLY37 MET375, ASN377 TYR380	−11.4	TYR255, ASN260 LYS280, PHE371 GLY374, MET375 ASN377, TYR380
4OW8	−8.3	LEU190, HIS192, ILE230, LYS255, ASN256	−8.1	LEU190, HIS192, ILE230, LYS255, ASN256
7P13	−9.7	THR262, GLU263 ASN266, TYR211 GLN214, TRP218	−10.5	LYS259, THR262 GLU263, ASN266 TYR211, GLN214 LEU215, TRP218 GLU263, LYS267
1IKQ	−7.5	HIS107, ASP139, ARG276, ARG279	−7.6	ASN215, GLU221, ASP403, GLN428
1EZM	−7.6	TRP115, ASP116, GLY117, TYR155	−7.7	TRP115, ASP116, GLY117, TYR155

Table 3. Binding affinities (kcal/mol) and interacting residues contributing to interaction of HO-C₆₀, [C₆₀]₂, and [C₆₀]₃ with 7D6Q, 7AHL, 4OW8, 1IKQ, and 1EZM receptors (R: receptor and IAA: interacting amino acid).

R	HO-C ₆₀	IAA	[C ₆₀] ₂	IAA	[C ₆₀] ₃	IAA
7D6Q	−9.7	LYS270, ILE271, ASN272, ASN273, LYS7, LEU44, THR45, GLY46, ASP70, ASN69, ASP70	−17.5	GLU211, ARG213, GLU215, ARG266, VAL268, LYS270, ASN272, ASN273, LEU275, LYS7, GLY46, ASN69, ASP70	−20.6	GLN173, ARG176, GLU177, GLN180, VAL188, TYR189, THR190, THR192, PRO193, GLY194, SER224, ASN226, ALA230, THR234, LYS5, LYS7, ASP24
1TII	−5.5	THR24, LYS25, SER42, THR43, GLY1, ALA98, ARG15, ARG141	15.9	GLU22, THR24, SER42, SER74, GLY75, MET76, ARG77, ALA98, ARG15 ARG16, GLY18, ALA28 ARG31, LEU119 ARG141, ASP142	185.6	GLU22, THR24, SER41, SER42, THR43, SER74, GLY75, MET76, ARG77, GLY1, ARG77, GLU97, ALA98, ARG15, ARG16, GLY18, LEU119, ARG139, ARG141, ASP142
7AHL	−12.9	ARG104, ASN105, SER106, ILE107, TYR102, PRO103, THR155, PHE224, ASP227	−19	ARG104, ASN105, SER106, ILE107 TYR102, PRO103, SER106, ILE107, ASP108, THR109, VAL149, THR155, PHE224, ASP227	−26.6	TYR118, PHE120, LEU116, TYR118, VAL140, HIS144, HIS144, GLN177, TRP179, PRO181, TYR182, TRP187, ASN188, GLN194, ARG200
1MWT	−9.8	TYR255, PRO258, ASN260, LYS280, PHE371, MET372, TYR373, GLY374, MET375, ASN377, TYR380	−17	ASN104, TYR105, ASN146, TRP205, LYS273, ASP274, ASP275, TYR297, THR308, ILE309	−22.7	ASN104, TYR105, GLU170, GLN203, TRP205, PRO213, ASN236, THR238, LYS273, ASP274, ASP275, TYR297, ILE309

Table 3. Cont.

R	HO-C ₆₀	IAA	[C ₆₀] ₂	IAA	[C ₆₀] ₃	IAA
4OW8	−8	TYR208, SER212, GLY213, LYS214, PRO235, PRO236, LEU237, PRO238	−12.6	SER212, LYS214, LYS228, GLU232, PRO235, PRO236, PRO238	−14.7	THR21, GLY22, GLY23, LYS45, PHE48, VAL166, GLY175, MET176, VAL177, MET178, GLY179, THR180, GLY221, ALA222
7P13	−9.7	THR262, GLU263, ASN266, TYR211, GLN214, LEU215, TRP218, GLU263, LYS267	−15.3	LYS259, THR262, GLU263, ASN266, LYS267, LYS207, TYR211, GLN214, TRP218	−20.2	THR262, ASN266, TYR211, GLN214, TRP218, LYS259, THR262, GLU263, ASN266, LYS267, GLN214, TRP218
1IKQ	−8.4	ASN215, GLU221, ASP403, GLN424, GLN428, ARG432	−12.6	GLU108, LYS185, ARG186, THR219, TRP281, GLU282, ASP406	−15.6	VAL351, ARG352, GLN353, GLU378, ILE465, PRO534, LEU535, PRO536, ARG538
1EZM	−7.9	TRP115, ASP116, GLY117, HIS144, TYR155, ASN163	−13.6	ASP48, TYR106, TYR114, TRP115, ASP116, GLY117, LEU121, TYR155	−18.1	ASP48, SER49, LYS103, TYR106, TYR114, TRP115, ASP116, THR118, LEU121, TYR155

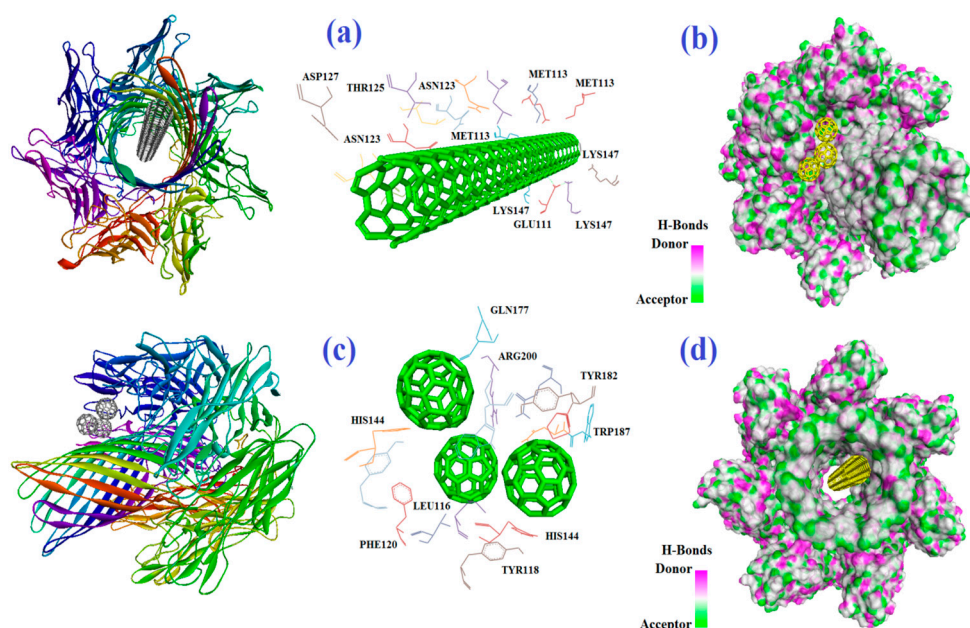


Figure 1. Interaction of CNT_{2–5} with 7AHL receptor (a), related donor and acceptor H-bonds of CNT_{2–5} (b), interaction of [C₆₀]₃ with 7AHL receptor (c), and related donor and acceptor H-bonds (d).

[C₆₀]₃ exhibited the best binding affinity toward alpha-hemolysin with a binding energy of −26.6 kcal/mol (Figure 1b). For the [C₆₀]₃–alpha-hemolysin complex, there were interacting amino acids including TYR118, PHE120, LEU116, TYR118, VAL140, HIS144, HIS144, GLN177, TRP179, PRO181, TYR182, TRP187, ASN188, GLN194, and ARG200 (Table 3). Capped CNTs showed −18.8 and −12.3 kcal/mol of binding energies for these virulence factors, respectively. In the case of 7AHL and capped CNTs, residues of LEU116, TYR118, VAL140, TYR112, HIS144, TRP179, PRO181, TYR182, SER186, TRP187, ASN188, PRO189, GLN194, ASN178, and TRP179 interacted at the binding site. There was no significant difference between C₆₀ and C₇₀ toward all receptors (Table 2). More affinity values of −12.8 and −13.6 kcal/mol were observed for C₆₀ and C₇₀ against 7AHL, respectively. Interacting amino acids ARG104, ASN105, SER106, ILE107, TYR102, PRO103, THR155,

PHE224, SER225, and ASP227 contributed to the interaction of C₇₀ with 7AHL. The interaction of C₆₀ with 7AHL showed ARG104, ASN105, SER106, ILE107, TYR102, PRO103, THR155, PHE224, SER225, and ASP227 interacting amino acids. Additionally, C₆₀ and C₇₀ had lower binding affinities (less than -8 kcal/mol) toward 1IKQ and 1EZM virulence factors. Therefore, results illustrated higher affinities of CNTs, capped CNTs, C₇₀, and C₆₀ toward alpha-hemolysin (7AHL) of *S. aureus* compared with other receptors by values of -19.6 , -18.8 , -13.6 , and -12.8 kcal/mol.

2.2. The Normal Mode Analysis

Frequency and deformation parameters were obtained with each normal mode analysis. In the case of deformation, simulation or the normal mode analysis of trajectories is critical to evaluate changes between two conformations. Moreover, the collective functional motions of biological macromolecules can be measured via normal mode analysis on the iMOD server [41]. The docking complex of CNT₂₋₅-alpha-hemolysin with the highest binding affinity was employed for the normal mode analysis study and molecular simulation using the iMOD and *ElNémo* servers. The molecular mobility (Figure 2a), main-chain deformability (Figure 2b), and B-factor (Figure 2c) were obtained for the complex of CNT₂₋₅-7AHL. There were locations with deformability in the regions of the 7AHL protein (Figure 2b). A stable structure for the CNT-1MWT complex was predicted with the B-factor analysis (Figure 2c) based on the mean of the root mean square (RMS). A variance plot (Figure 3a), eigenvalue (Figure 3b), covariance map (Figure 3c), and elastic network model (Figure 3d) were obtained for the normal modes. The easier deformation of the macromolecule can be predicted by a lower value of the eigenvalue. The eigenvalue for each normal mode showed motion stiffness at a value of 1.345×10^{-4} (Figure 3b). Red, white, and blue colors exhibit correlated, uncorrelated, and anti-correlated motions, respectively, based on the covariance matrix analysis (Figure 3c). Additionally, the rigidity and flexibility of springs between (C α) atoms of docked protein molecules are indicated with darker and brighter colors (Figure 3d) [42]. To clarify the conformational change of the CNT₂₋₅-7AHL complex, snapshots at frame 1, frame 5, and frame 11 are illustrated in Figure 4 [43]. The root mean square deviation (RMSD) of ligand atoms can show the stability level of a docked complex [44]. CNT₂₋₅ exhibited stability within the active site with an average of 0.765 ± 0.42 Å of RMSD.

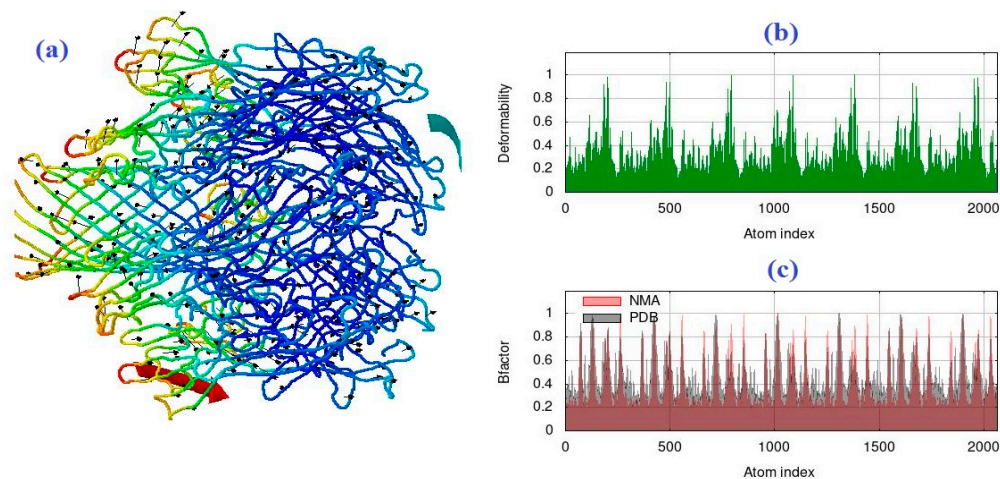


Figure 2. Molecular mobility. (a) (Two colored affine arrows showing the domain's mobility) the main-chain deformability, and (b,c) B-factor evaluated with the NMA of the main docked complex of CNT₂₋₅-7AHL.

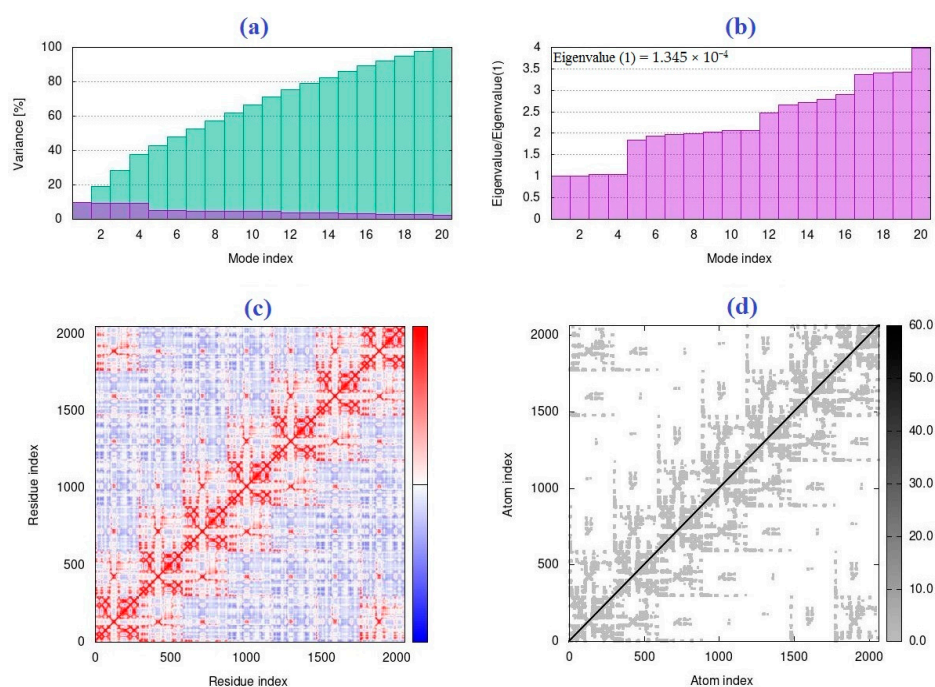


Figure 3. Results of iMODS for variance plot (a), colored bars show the cumulative (green) and individual (purple), variances, eigenvalue (b), covariance matrix analysis (c), and elastic network model (d) for CNT₂₋₅-7AHL.

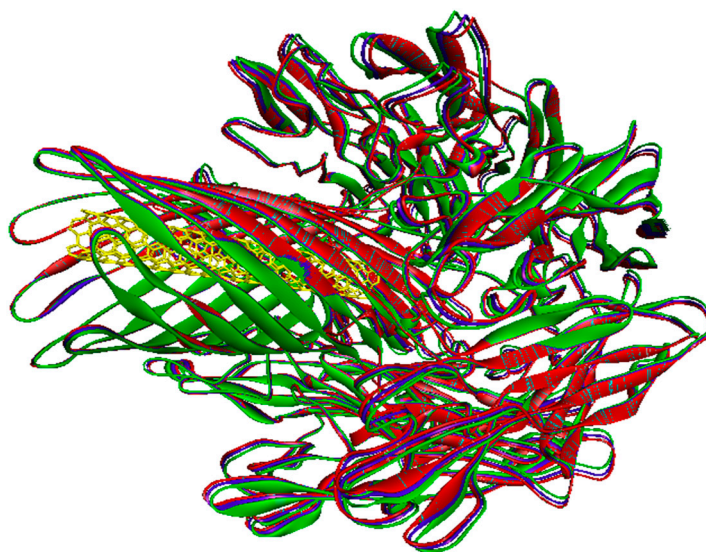


Figure 4. The aligned structures of CNT₂₋₅-7AHL during simulation at frame 1 (red), frame 5 (blue), and frame 11 (green) based on the results of the *Elnémo* server. CNT₂₋₅ has shown in the yellow color.

3. Discussion

This *in silico* study showed more affinity of CNTs, capped CNTs, CNT₂₋₅, C₇₀, C₆₀, HO-C₆₀, [C₆₀]₂, and [C₆₀]₃ toward alpha-hemolysin (7AHL) of *S. aureus* compared to other virulence factors with values of -19.6 , -18.8 , -32.7 , -13.6 , -12.8 , -12.9 , -19 , and -26.6 kcal/mol, respectively. Among all receptors, the lowest and highest binding affinities were found for CNTs against 1TII and 1MWT with binding energy values of 97.4 and -20.1 kcal/mol. Moreover, C₆₀ and C₇₀ had lower binding affinities (less than -8 kcal/mol) toward 1IKQ and 1EZM virulence factors. In a similar study, the docking of fullerene C₆₀ against several receptors of drug-resistant *Salmonella typhi* was evaluated with AutoDock Vina. This study disclosed that C₆₀ can form a stable interaction with

receptors of *ssrB*, *slrP*, and *PhoQ* with values of -12.9 , -12.8 , and -12.2 kcal/mol, respectively. For the interaction of C_{60} with *ssrB*, the interacting amino acids were Gly 116, Arg 186, Pro 238, Pro 278, and Pro 281 [45]. The antimicrobial activities of CNTs and fullerene have been reported in several studies [46,47]. Physical membrane damage, the production of reactive oxygen species, and the disruption of metabolic pathways are the main antibacterial mechanisms of CNTs. The antibacterial activity of CNTs can be affected by their diameter, length, surface chemistry, and surface functional group properties. In addition, the characteristics of bacteria, including type and morphology, mechanical properties of the cell wall, and growth state (planktonic and biofilm forms), can determine the antibacterial capacity of CNTs. In addition, the surface modification of CNTs using antimicrobial compounds, metal/metal oxide NPs, amino acids, and polymers has shown different antibacterial activities, including the inhibition of the cell wall, oxidative stress, and the promotion of the contact between CNTs or MWCNTs and the bacterial cell wall [48]. It should be noted that the antibacterial activity of carbon nanomaterials is found in their composition, surface modification, and target bacteria [49]. *E. coli* and *Salmonella typhimurium* were inhibited via functionalized MWCNTs with lysine and arginine. The increased antibacterial activity of this nanocomposite resulted from the electrostatic adsorption of bacteria membranes because of the positive charges of lysine and arginine on MWCNT surfaces [50]. The 3D nanostructures composed of graphene-carbon nanotubes-iron oxides had higher adsorption and antibacterial capacity toward *E. coli* and *S. aureus* [51]. The thin film based on polymer-shielded Ag nanoparticle-loaded oxidized CNTs prepared via spray-assisted layer-by-layer assembly showed significant antibacterial activity against Gram-positive *S. aureus* and Gram-negative *E. coli* [52]. Antibiotics may be used to surface-functionalize CNTs or MWCNTs and synergize their antibacterial activity. In this way, covalent grafting of antibiotics with surface-modified CNTs was applied to conjugate levofloxacin with MWCNTs. In low effective doses, there was a higher sensitivity of *S. aureus* compared to *Pseudomonas aeruginosa*. This may result from the different cell wall morphologies of Gram-negative and Gram-positive bacteria [53]. In infected chronic wounds and septicemia, hindering and eradicating bacterial growth in physiological conditions is a critical issue [54,55]. For this aspect, to increase the cellular uptake of CNTs and capped CNTs, other surface functionalization strategies, including shortened CNTs bifunctionalized with amphotericin B, CNTs bifunctionalized with ammonium groups, ammonium-functionalized CNTs, CNTs functionalized with fluorescein isothiocyanate and acetamido-functionalized CNTs, and CNTs bifunctionalized with methotrexate, can be considered for future investigations [56]. The major limitation of the antibacterial efficiency of fullerene is its hydrophobicity, which can be improved via surface functionalization, including esterification (fullerene-COOR), carboxylation (fullerene-COOH), and hydroxylation (fullerene-OH). An increased hydrophilic property augmented the contact between lysozyme and fullerene, which was followed by more conformational changes and a significant antibacterial effect [57]. Moreover, other derivatives of C_{60} fullerene, such as fulleropyrrolidine C_{60} and dicationic fulleropyrrolidinium, have exhibited supreme bactericidal activity against Gram-negative and Gram-positive bacteria [28]. It should be noted that pristine C_{60} fullerene aggregate stabilization in an aqueous medium can result from the surface hydroxylation of C_{60} fullerene [58]. Moreover, the functionalization of fullerenol (polyhydroxylated fullerene) with the antibacterial drug sulfasalazine caused increased antibacterial activity against both Gram-negative and Gram-positive bacteria [59]. Higher polarizabilities and surface areas of CNT_{2-5} and $[C_{60}]_3$ compared to CNTs and fullerene may be the main reasons for increasing their reactivity and interaction with alpha-hemolysin [49,60,61]. Bacterial pathogenesis produced by various virulence factors, including secretory, membrane-associated, or cytosolic forms, can colonize and damage the host cells [62]. For example, in the case of *M. tuberculosis*, protein kinase A is a critical factor for growth and has been considered a possible drug target [63]. *Pseudomonas elastase* is a major virulence factor in *P. aeruginosa* that is regulated with the *lasR* gene and leads to extensive tissue damage [64]. Exotoxin A of *P. aeruginosa* inhibits protein

synthesis and interferes with cellular immune functions [65]. Alpha-hemolysin of *S. aureus*, a pore-forming toxin, can penetrate cell membranes and lead to the osmotic swelling and lysis of erythrocytes [66]. Gastrointestinal disease and hemolytic uremic syndrome can result from shiga toxin 2a of *E. coli* [67].

The application of carbon nanomaterials such as graphenes, fullerenes, and CNTs in 3D-printed scaffolds is increasing because of their biocompatibility and their therapeutic, electrical, mechanical, and thermomechanical properties. Electrical stimulation can impact human cell viability and the bacterial growth of Gram-negative and Gram-positive bacteria. In this regard, 3D-printed electroactive scaffolds composed of polycaprolactone and conductive thermally reduced graphene oxide (TrGO) nanoparticles showed significant antibacterial activity against *S. aureus* on the surface of scaffolds [68]. In the case of MWCNTs, there were increased thermomechanical and mechanical properties for the 5.0 wt.% filler's ratio of the polyamide 12 (PA12)/MWCNT nanocomposite (5.0% wt.% incorporation of MWCNTs into the PA12). By increasing the filler's ratio to 10% wt.%, the electrical conductivity was increased. The growth of *E. coli* and *S. aureus* was inhibited at inhibition zone diameters of 2.1 and 2.5 mm, respectively, with the 3D-printed PA12/MWCNT 10.0 wt.% nanocomposite specimen after 24 h of incubation [69]. It should be noted that understanding and reducing the cytotoxicity of CNTs is a crucial step before their therapeutic application. Indeed, there are key factors, including synthesis and impurity content, purification and sorting, length and aggregation, biomolecule corona, covalent functionalization, and non-covalent encapsulation, related to SWCNT cellular toxicity. However, we can attempt to reduce SWCNT cellular toxicity with several strategies such as controlling the synthesis process for hindering aggregation and impurity and surface modification by biocompatible materials [70,71].

4. Materials and Methods

4.1. Molecular Docking Preparation

Virulence factors of *E. coli*; shiga toxin 2a (ID: 7D6Q and resolution: 1.80 Å) and heat-labile enterotoxin (ID: 1TII and resolution: 2.25 Å), *S. aureus*; alpha-hemolysin (ID: 7AHL and resolution: 1.89 Å) and penicillin-binding protein 2a (ID: 1MWT and resolution: 2.45 Å), *M. tuberculosis*; protein kinase A (ID: 4OW8 and resolution: 2.03 Å) and mycobacterial ESX-secreted protein B (ID: 7P13 and resolution: 2.29 Å), *P. aeruginosa*; and elastase (ID: 1EZM and resolution: 1.50 Å) and exotoxin A (1IKQ and resolution: 1.62 Å) (Figure 5a–h) were obtained from the Research Collaboratory for Structural Bioinformatics (RCSB) as the receptors (<http://www.rcsb.org/>; accessed on 20 December 2022). Grid box parameters (7D6Q; center_x = 2.95, center_y = 33.76, center_z = 0.39, size_x = 68, size_y = 94, and size_z = 62 Å), (7AHL; center_x = 49.29, center_y = 32.77, center_z = 42.17, size_x = 92, size_y = 76, and size_z = 92 Å), (4OW8; center_x = -2.54, center_y = 6.46, center_z = -18.05, size_x = 54, size_y = 40, and size_z = 44 Å), (1EZM; center_x = 45.75, center_y = 33.09, center_z = 28.00, size_x = 40, size_y = 58, and size_z = 46 Å), and (1IKQ; center_x = 32.10, center_y = 36.45, center_z = 16.80, size_x = 78, size_y = 56, and size_z = 60 Å) were determined with AutoDock Vina 1.1.2 based on blind docking [72]. Armchair CNT (5,5) and capped CNT ligands with a diameter of ~1 nm and a length of ~2 nm, CNT₂₋₅ with a diameter of ~2 nm and a length of ~5 nm, as well as C₆₀, C₇₀, HO-C₆₀, [C₆₀]₂, and [C₆₀]₃ with a diameter of ~1 nm were prepared via material studio 2017 for the evaluation of a ligand–receptor interaction (Figure 6a–h) [61,73]. The UCSF Chimera1.12 program was used to prepare the optimized structures of ligands, followed by removing all the water molecules. Molecular dockings of a ligand–receptor interaction and visualization of the results were carried out using the ADV1.1.2 and Discovery Studio Visualizer (DSV) 2016 [74].

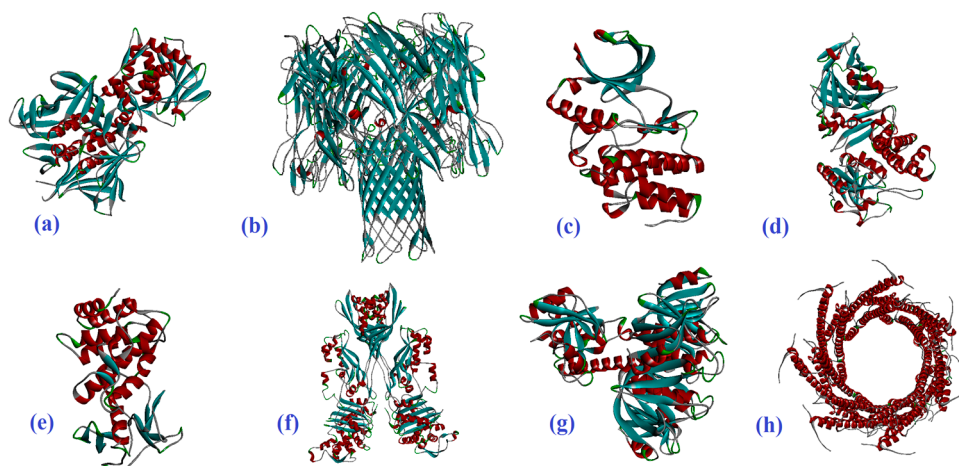


Figure 5. (a) 7D6Q, (b) 7AHL, (c) 4OW8, (d) 1IKQ, (e) 1EZM, (f) 1MWT, (g) 1TII, and (h) 7P13.

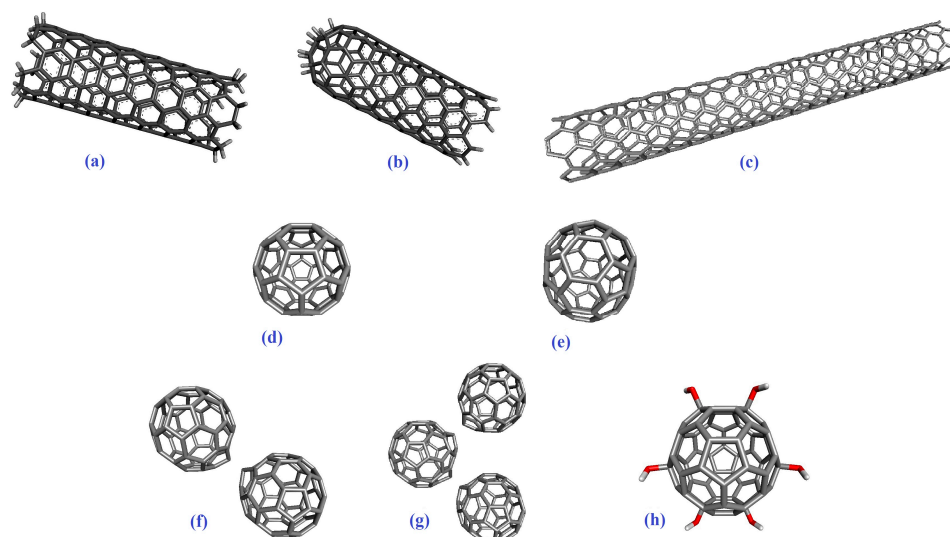


Figure 6. (a) Armchair CNT (5,5), (b) capped CNT, (c) CNT₂₋₅, (d) C₆₀, (e) C₇₀, (f) [C₆₀]₂, (g) [C₆₀]₃, and (h) HO-C₆₀.

4.2. The Normal Mode Analysis

Each normal mode for the collective functional motions of biological macromolecules comprises a frequency and a deformation, which can be evaluated with the iMOD server. The iMOD server can provide simulation or normal mode analysis of trajectories between two conformations interactively. Since molecular docking may not be fully reliable, molecular dynamic simulation of the prominent docking interaction was selected to obtain the normal mode analysis study [41]. The structural dynamics and molecular motion of the docking complex were evaluated via the iMOD server [75]. The covariance map, complex deformability, elastic network, B-factor, eigenvalues, and variance can be indicated with this web server [76]. The results were presented with all the parameters set to default [77]. Additionally, the elastic network model of the *EINémo* server was used to evaluate the contribution of each normal mode to its conformational change for a main docked interaction with the highest binding energy [78].

5. Conclusions

The results of the docking study obtained from AutoDock Vina disclosed that CNTs compared to fullerenes had more affinity for bacterial virulence factors, which can be attributed to the different morphology of CNTs (tubular shape) compared to fullerenes (spherical shape). This study exhibited more affinity of CNTs, capped CNTs, CNT₂₋₅, C₇₀,

C₆₀, HO-C₆₀, [C₆₀]₂, and [C₆₀]₃ toward alpha-hemolysin (7AHL) of *S. aureus* compared to other virulence factors, respectively. Methionine (MET113) and glutamine (GLU111) were found specifically for the CNT₂₋₅-7AHL docking complex, with the lowest binding energy of −32.7 kcal/mol. Additionally, the desirable conformational change and stability of the CNT-1MWT complex at different times were indicated according to the normal mode analysis of the *ElNémo* server and iMODS. For future studies, improving the cellular uptake of CNTs and capped CNTs via surface functionalization with ammonium and acetamide groups can be effective strategies. In the case of fullerenes, esterification (fullerene-COOR), carboxylation (fullerene-COOH), and hydroxylation (fullerene-OH) can be regarded as ways to increase their hydrophilicity. In addition, loading some antibiotics, such as sulfasalazine, on the polyhydroxylated fullerene can be an effective strategy. The application of positive functional groups on the surface of CNTs, such as lysine and arginine, can improve antibacterial activity resulting from the electrostatic adsorption of bacteria membranes with negative charges. Additionally, various antibiotics may be applied to surface-functionalize CNTs and synergize their antibacterial activity against Gram-negative and Gram-positive bacteria. These carbon-based nano-antibiotics have major industrialization potential with low toxicity and are suitable for wound infections. Generally, the antibacterial activity of carbon nanomaterials is found in their composition, surface modification, and target bacteria. Therefore, future *in silico* and *in vitro* studies should be focused on the antibacterial activity of surface-functionalized CNTs and fullerenes.

Author Contributions: Conceptualization, M.A. (Mehran Alavi) and M.A. (Morahem Ashengroph); methodology, M.A. (Mehran Alavi); software, M.A. (Mehran Alavi); validation, M.A. (Mehran Alavi) and M.A. (Morahem Ashengroph); formal analysis, M.A. (Mehran Alavi); resources, M.A. (Morahem Ashengroph); data curation, M.A. (Mehran Alavi); writing—original draft preparation, M.A. (Mehran Alavi); review and editing, M.A. (Mehran Alavi) and M.R.M.; visualization, M.A. (Mehran Alavi) and M.R.M.; supervision, M.A. (Morahem Ashengroph). All authors have read and agreed to the published version of the manuscript.

Funding: This study was supported by the Research Council of the University of Kurdistan for their financial support under Grant Agreement Number 00/9/34027/2021.

Data Availability Statement: The data presented in this study are available in article.

Conflicts of Interest: The authors declare no conflicts of interest.

References

1. Amraei, S.; Eslami, G.; Taherpour, A.; Hashemi, A. Relationship between MOX genes and antibiotic resistance in *Klebsiella pneumoniae* strains in nosocomial infections. *Micro Nano Bio Asp.* **2022**, *1*, 12–17. [[CrossRef](#)]
2. Amraei, S.; Eslami, G.; Taherpour, A.; Hashemi, A. The role of ACT and FOX genes in *Klebsiella pneumoniae* strains isolated from hospitalized patients. *Micro Nano Bio Asp.* **2022**, *1*, 18–25. [[CrossRef](#)]
3. Amraei, S.; Ahmadi, S. Recent studies on antimicrobial and anticancer activities of saponins: A mini-review. *Nano Micro Biosyst.* **2022**, *1*, 22–26. [[CrossRef](#)]
4. Alavi, M.; Jabari, E.; Jabbari, E. Functionalized carbon-based nanomaterials and quantum dots with antibacterial activity: A review. *Expert Rev. Anti Infect. Ther.* **2021**, *19*, 35–44. [[CrossRef](#)] [[PubMed](#)]
5. Zheng, S.; Tian, Y.; Ouyang, J.; Shen, Y.; Wang, X.; Luan, J. Carbon nanomaterials for drug delivery and tissue engineering. *Front. Chem.* **2022**, *10*, 990362. [[CrossRef](#)] [[PubMed](#)]
6. Riha, S.M.; Maarof, M.; Fauzi, M.B. Synergistic Effect of Biomaterial and Stem Cell for Skin Tissue Engineering in Cutaneous Wound Healing: A Concise Review. *Polymers* **2021**, *13*, 1546. [[CrossRef](#)]
7. Qiu, Y.L.; Chen, X.; Hou, Y.L.; Hou, Y.J.; Tian, S.B.; Chen, Y.H.; Yu, L.; Nie, M.H.; Liu, X.Q. Characterization of different biodegradable scaffolds in tissue engineering. *Mol. Med. Rep.* **2019**, *19*, 4043–4056. [[CrossRef](#)] [[PubMed](#)]
8. Khurshid, Z.; Husain, S.; Alotaibi, H.; Rehman, R.; Zafar, M.S.; Farooq, I.; Khan, A.S. Chapter 18-Novel Techniques of Scaffold Fabrication for Bioactive Glasses. In *Biomedical, Therapeutic and Clinical Applications of Bioactive Glasses*; Kaur, G., Ed.; Woodhead Publishing: Sawston, UK, 2019; pp. 497–519. [[CrossRef](#)]
9. Suamte, L.; Tirkey, A.; Barman, J.; Jayasekhar Babu, P. Various manufacturing methods and ideal properties of scaffolds for tissue engineering applications. *Smart Mater. Manuf.* **2023**, *1*, 100011. [[CrossRef](#)]
10. Kołbuk, D.; Heljak, M.; Choińska, E.; Urbanek, O. Novel 3D Hybrid Nanofiber Scaffolds for Bone Regeneration. *Polymers* **2020**, *12*, 544. [[CrossRef](#)]

11. Chung, J.J.; Im, H.; Kim, S.H.; Park, J.W.; Jung, Y. Toward Biomimetic Scaffolds for Tissue Engineering: 3D Printing Techniques in Regenerative Medicine. *Front. Bioeng. Biotechnol.* **2020**, *8*, 586406. [[CrossRef](#)]
12. Qu, M.; Wang, C.; Zhou, X.; Libanori, A.; Jiang, X.; Xu, W.; Zhu, S.; Chen, Q.; Sun, W.; Khademhosseini, A. Multi-Dimensional Printing for Bone Tissue Engineering. *Adv. Healthc. Mater.* **2021**, *10*, 2001986. [[CrossRef](#)]
13. Shahrubudin, N.; Lee, T.C.; Ramlan, R. An Overview on 3D Printing Technology: Technological, Materials, and Applications. *Procedia Manuf.* **2019**, *35*, 1286–1296. [[CrossRef](#)]
14. Bhagia, S.; Bornani, K.; Agrawal, R.; Satlewal, A.; Đurković, J.; Lagaña, R.; Bhagia, M.; Yoo, C.G.; Zhao, X.; Kunc, V.; et al. Critical review of FDM 3D printing of PLA biocomposites filled with biomass resources, characterization, biodegradability, upcycling and opportunities for biorefineries. *Appl. Mater. Today* **2021**, *24*, 101078. [[CrossRef](#)]
15. Zhao, Y.-Q.; Yang, J.-H.; Ding, X.; Ding, X.; Duan, S.; Xu, F.-J. Polycaprolactone/polysaccharide functional composites for low-temperature fused deposition modelling. *Bioact. Mater.* **2020**, *5*, 185–191. [[CrossRef](#)] [[PubMed](#)]
16. Wasserfall, F.; Hendrich, N.; Ahlers, D.; Zhang, J. Topology-aware routing of 3D-printed circuits. *Addit. Manuf.* **2020**, *36*, 101523. [[CrossRef](#)]
17. Cui, M.; Pan, H.; Su, Y.; Fang, D.; Qiao, S.; Ding, P.; Pan, W. Opportunities and challenges of three-dimensional printing technology in pharmaceutical formulation development. *Acta Pharm. Sin. B* **2021**, *11*, 2488–2504. [[CrossRef](#)] [[PubMed](#)]
18. Abdullah, T.; Qurban, R.O.; Bolarinwa, S.O.; Mirza, A.A.; Pasovic, M.; Memic, A. 3D Printing of Metal/Metal Oxide Incorporated Thermoplastic Nanocomposites with Antimicrobial Properties. *Front. Bioeng. Biotechnol.* **2020**, *8*, 568186. [[CrossRef](#)] [[PubMed](#)]
19. Patila, M.; Chalmes, N.; Dounousi, E.; Stamatis, H.; Gournis, D. Chapter Twelve—Use of functionalized carbon nanotubes for the development of robust nanobiocatalysts. In *Methods Enzymology*; Kumar, C.V., Ed.; Academic Press: Cambridge, MA, USA, 2020; Volume 630, pp. 263–301.
20. Ardeshana, B.; Jani, U.; Patel, A. Influence of Bending Angle on Mechanical Performance of SWCNTs and DWCNTs Based on Molecular Mechanics: FE Approach. *J. Vib. Eng. Technol.* **2022**, *11*, 251–264. [[CrossRef](#)]
21. Nadeem, M.F.; Azeem, M.; Farman, I. Comparative study of topological indices for capped and uncapped carbon nanotubes. *Polycycl. Aromat. Compd.* **2022**, *42*, 4666–4683. [[CrossRef](#)]
22. Cui, H.; Yu, Y.; Li, X.; Sun, Z.; Ruan, J.; Wu, Z.; Qian, J.; Yin, J. Direct 3D printing of a tough hydrogel incorporated with carbon nanotubes for bone regeneration. *J. Mater. Chem. B* **2019**, *7*, 7207–7217. [[CrossRef](#)]
23. Li, L.; Qin, S.; Peng, J.; Chen, A.; Nie, Y.; Liu, T.; Song, K. Engineering gelatin-based alginate/carbon nanotubes blend bioink for direct 3D printing of vessel constructs. *Int. J. Biol. Macromol.* **2020**, *145*, 262–271. [[CrossRef](#)]
24. Young, Y.-F.; Lee, H.-J.; Shen, Y.-S.; Tseng, S.-H.; Lee, C.-Y.; Tai, N.-H.; Chang, H.-Y. Toxicity mechanism of carbon nanotubes on *Escherichia coli*. *Mater. Chem. Phys.* **2012**, *134*, 279–286. [[CrossRef](#)]
25. Sui, M.; Zhang, L.; Sheng, L.; Huang, S.; She, L. Synthesis of ZnO coated multi-walled carbon nanotubes and their antibacterial activities. *Sci. Total Environ.* **2013**, *452–453*, 148–154. [[CrossRef](#)]
26. Kang, S.; Pinault, M.; Pfefferle, L.D.; Elimelech, M. Single-Walled Carbon Nanotubes Exhibit Strong Antimicrobial Activity. *Langmuir* **2007**, *23*, 8670–8673. [[CrossRef](#)] [[PubMed](#)]
27. Zhu, B.; Xia, X.; Xia, N.; Zhang, S.; Guo, X. Modification of Fatty Acids in Membranes of Bacteria: Implication for an Adaptive Mechanism to the Toxicity of Carbon Nanotubes. *Environ. Sci. Technol.* **2014**, *48*, 4086–4095. [[CrossRef](#)] [[PubMed](#)]
28. Hou, W.; Shi, G.; Wu, S.; Mo, J.; Shen, L.; Zhang, X.; Zhu, Y. Application of Fullerenes as Photosensitizers for Antimicrobial Photodynamic Inactivation: A Review. *Front. Microbiol.* **2022**, *13*, 957698. [[CrossRef](#)] [[PubMed](#)]
29. Wang, Y.; Yang, Y.; Shi, Y.; Song, H.; Yu, C. Antibiotic-Free Antibacterial Strategies Enabled by Nanomaterials: Progress and Perspectives. *Adv. Mater.* **2020**, *32*, 1904106. [[CrossRef](#)] [[PubMed](#)]
30. Hada, V.; Chaturvedi, K.; Singhwane, A.; Siraj, N.; Gupta, A.; Sathish, N.; Chaurasia, J.P.; Srivastava, A.K.; Verma, S. Nanoantibiotic effect of carbon-based nanocomposites: Epicentric on graphene, carbon nanotubes and fullerene composites: A review. *3 Biotech* **2023**, *13*, 147. [[CrossRef](#)] [[PubMed](#)]
31. Krishna, R.H.; Chandraprabha, M.N.; Monika, P.; Br, T.; Chaudhary, V.; Manjunatha, C. Biomolecule conjugated inorganic nanoparticles for biomedical applications: A review. *Biotechnol. Genet. Eng. Rev.* **2022**, 1–42. [[CrossRef](#)] [[PubMed](#)]
32. Abdelsattar, A.S.; Dawoud, A.; Helal, M.A. Interaction of nanoparticles with biological macromolecules: A review of molecular docking studies. *Nanotoxicology* **2021**, *15*, 66–95. [[CrossRef](#)] [[PubMed](#)]
33. Ghanem, S.M.; Abd El-Baky, R.M.; Abourehab, M.A.S.; Fadl, G.F.M.; Gamil, N.G.F.M. Prevalence of Quorum Sensing and Virulence Factor Genes among *Pseudomonas aeruginosa* Isolated from Patients Suffering from Different Infections and Their Association with Antimicrobial Resistance. *Infect. Drug Resist.* **2023**, *16*, 2371–2385. [[CrossRef](#)] [[PubMed](#)]
34. Gupta, P.; Gupta, R.K.; Harjai, K. Multiple virulence factors regulated by quorum sensing may help in establishment and colonisation of urinary tract by *Pseudomonas aeruginosa* during experimental urinary tract infection. *Indian J. Med. Microbiol.* **2013**, *31*, 29–33. [[CrossRef](#)]
35. Seilie, E.S.; Bubeck Wardenburg, J. *Staphylococcus aureus* pore-forming toxins: The interface of pathogen and host complexity. *Semin. Cell Dev. Biol.* **2017**, *72*, 101–116. [[CrossRef](#)]
36. Fishovitz, J.; Hermoso, J.A.; Chang, M.; Mobashery, S. Penicillin-binding protein 2a of methicillin-resistant *Staphylococcus aureus*. *IUBMB Life* **2014**, *66*, 572–577. [[CrossRef](#)] [[PubMed](#)]

37. Malhotra, V.; Okon, B.P.; Satsangi, A.T.; Das, S.; Waturoocha, U.W.; Vashist, A.; Clark-Curtiss, J.E.; Saini, D.K. Mycobacterium tuberculosis PknK Substrate Profiling Reveals Essential Transcription Terminator Protein Rho and Two-Component Response Regulators PrrA and MtrA as Novel Targets for Phosphorylation. *Microbiol. Spectr.* **2022**, *10*, e01354-21. [[CrossRef](#)] [[PubMed](#)]
38. Gijbsbers, A.; Vinciauskaite, V.; Siroy, A.; Gao, Y.; Tria, G.; Mathew, A.; Sánchez-Puig, N.; López-Iglesias, C.; Peters, P.J.; Ravelli, R.B.G. Priming mycobacterial ESX-secreted protein B to form a channel-like structure. *Curr. Res. Struct. Biol.* **2021**, *3*, 153–164. [[CrossRef](#)] [[PubMed](#)]
39. Schuetz, A.N. Emerging agents of gastroenteritis: Aeromonas, Plesiomonas, and the diarrheagenic pathotypes of *Escherichia coli*. *Semin. Diagn. Pathol.* **2019**, *36*, 187–192. [[CrossRef](#)]
40. Johura, F.-T.; Parveen, R.; Islam, A.; Sadique, A.; Rahim, M.N.; Monira, S.; Khan, A.R.; Ahsan, S.; Ohnishi, M.; Watanabe, H.; et al. Occurrence of Hybrid *Escherichia coli* Strains Carrying Shiga Toxin and Heat-Stable Toxin in Livestock of Bangladesh. *Front. Public Health* **2017**, *4*, 287. [[CrossRef](#)]
41. López-Blanco, J.R.; Aliaga, J.I.; Quintana-Ortí, E.S.; Chacón, P. iMODS: Internal coordinates normal mode analysis server. *Nucleic Acids Res.* **2014**, *42*, W271–W276. [[CrossRef](#)]
42. Bhattacharjee, M.; Banerjee, M.; Mukherjee, A. In silico designing of a novel polyvalent multi-subunit peptide vaccine leveraging cross-immunity against human visceral and cutaneous leishmaniasis: An immunoinformatics-based approach. *J. Mol. Model.* **2023**, *29*, 99. [[CrossRef](#)]
43. Bauer, J.A.; Pavlović, J.; Bauerová-Hlinková, V. Normal Mode Analysis as a Routine Part of a Structural Investigation. *Molecules* **2019**, *24*, 3293. [[CrossRef](#)]
44. Al-Karmalawy, A.A.; Alnajjar, R.; Dahab, M.; Metwaly, A.; Eissa, I. Molecular docking and dynamics simulations reveal the potential of anti-HCV drugs to inhibit COVID-19 main protease. *Pharm. Sci.* **2021**, *27*, S109–S121. [[CrossRef](#)]
45. Skariyachan, S.; Parveen, A.; Garka, S. Nanoparticle Fullerene (C60) demonstrated stable binding with antibacterial potential towards probable targets of drug resistant *Salmonella typhi*—A computational perspective and in vitro investigation. *J. Biomol. Struct. Dyn.* **2017**, *35*, 3449–3468. [[CrossRef](#)] [[PubMed](#)]
46. Ahmed, L.; Rasulev, B.; Turabekova, M.; Leszczynska, D.; Leszczynski, J. Receptor-and ligand-based study of fullerene analogues: Comprehensive computational approach including quantum-chemical, QSAR and molecular docking simulations. *Org. Biomol. Chem.* **2013**, *11*, 5798–5808. [[CrossRef](#)] [[PubMed](#)]
47. Gopal, D.; Skariyachan, S.; Melappa, G. Chapter 8-Molecular interaction modeling of carbon nanotubes and fullerene toward prioritized targets of SARS-CoV-2 by computer-aided screening and docking studies. In *Functionalized Carbon Nanomaterials for Theranostic Applications*; Mallakpour, S., Hussain, C.M., Eds.; Elsevier: Amsterdam, The Netherlands, 2023; pp. 157–179. [[CrossRef](#)]
48. Teixeira-Santos, R.; Gomes, M.; Gomes, L.C.; Mergulhão, F.J. Antimicrobial and anti-adhesive properties of carbon nanotube-based surfaces for medical applications: A systematic review. *iScience* **2021**, *24*, 102001. [[CrossRef](#)] [[PubMed](#)]
49. Azizi-Lalabadi, M.; Hashemi, H.; Feng, J.; Jafari, S.M. Carbon nanomaterials against pathogens; the antimicrobial activity of carbon nanotubes, graphene/graphene oxide, fullerenes, and their nanocomposites. *Adv. Colloid Interface Sci.* **2020**, *284*, 102250. [[CrossRef](#)] [[PubMed](#)]
50. Zardini, H.Z.; Amiri, A.; Shanbedi, M.; Maghrebi, M.; Baniadam, M. Enhanced antibacterial activity of amino acids-functionalized multi walled carbon nanotubes by a simple method. *Colloids Surf. B Biointerfaces* **2012**, *92*, 196–202. [[CrossRef](#)] [[PubMed](#)]
51. Sharma, V.K.; McDonald, T.J.; Kim, H.; Garg, V.K. Magnetic graphene–carbon nanotube iron nanocomposites as adsorbents and antibacterial agents for water purification. *Adv. Colloid Interface Sci.* **2015**, *225*, 229–240. [[CrossRef](#)] [[PubMed](#)]
52. Nie, C.; Yang, Y.; Cheng, C.; Ma, L.; Deng, J.; Wang, L.; Zhao, C. Bioinspired and biocompatible carbon nanotube-Ag nanohybrid coatings for robust antibacterial applications. *Acta Biomater.* **2017**, *51*, 479–494. [[CrossRef](#)]
53. Hassani, M.; Tahghighi, A.; Rohani, M.; Hekmati, M.; Ahmadian, M.; Ahmadvand, H. Robust antibacterial activity of functionalized carbon nanotube-levofloxacin conjugate based on in vitro and in vivo studies. *Sci. Rep.* **2022**, *12*, 10064. [[CrossRef](#)]
54. Alavi, M.; Hamblin, M.R. Interaction of copper oxide nanoparticles with bacterial nucleic acids: A mini-review. *Micro Nano Bio Asp.* **2023**, *2*, 20–25. [[CrossRef](#)]
55. Aljelehaw, Q.; Maroufi, Y.; Javid, H.; Mohammadi, M.R.; Raji Mal Allah, O.; Taheri, S.V.; Mohammadzade, H. Anticancer, antineurodegenerative, antimicrobial, and antidiabetic activities of carvacrol: Recent advances and limitations for effective formulations. *Nano Micro Biosyst.* **2023**, *2*, 1–10. [[CrossRef](#)]
56. Kostarelos, K.; Lacerda, L.; Pastorin, G.; Wu, W.; Wieckowski, S.; Luangsivilay, J.; Godefroy, S.; Pantarotto, D.; Briand, J.-P.; Muller, S.; et al. Cellular uptake of functionalized carbon nanotubes is independent of functional group and cell type. *Nat. Nanotechnol.* **2007**, *2*, 108–113. [[CrossRef](#)] [[PubMed](#)]
57. Bai, Y.; Wu, X.; Ouyang, P.; Shi, M.; Li, Q.; Maimaiti, T.; Lan, S.; Yang, S.-T.; Chang, X.-L. Surface modification mediates the interaction between fullerene and lysozyme: Protein structure and antibacterial activity. *Environ. Sci. Nano* **2021**, *8*, 76–85. [[CrossRef](#)]
58. Prylutskyy, Y.I.; Petrenko, V.I.; Ivankov, O.I.; Kyzyma, O.A.; Bulavin, L.A.; Litsis, O.O.; Evstigneev, M.P.; Cherepanov, V.V.; Naumovets, A.G.; Ritter, U. On the Origin of C60 Fullerene Solubility in Aqueous Solution. *Langmuir* **2014**, *30*, 3967–3970. [[CrossRef](#)] [[PubMed](#)]

59. Javed Ansari, M.; Soltani, A.; Ramezanitaghartapeh, M.; Singla, P.; Aghaei, M.; Khandan Fadafan, H.; Ardalan Khales, S.; Shariati, M.; Shirzad-Aski, H.; Balakheyli, H.; et al. Improved antibacterial activity of sulfasalazine loaded fullerene derivative: Computational and experimental studies. *J. Mol. Liq.* **2022**, *348*, 118083. [[CrossRef](#)]
60. Lyon, D.Y.; Adams, L.K.; Falkner, J.C.; Alvarez, P.J. Antibacterial activity of fullerene water suspensions: Effects of preparation method and particle size. *Environ. Sci. Technol.* **2006**, *40*, 4360–4366. [[CrossRef](#)] [[PubMed](#)]
61. Sabirov, D.S. Polarizability of C60 fullerene dimer and oligomers: The unexpected enhancement and its use for rational design of fullerene-based nanostructures with adjustable properties. *RSC Adv.* **2013**, *3*, 19430–19439. [[CrossRef](#)]
62. Qin, S.; Xiao, W.; Zhou, C.; Pu, Q.; Deng, X.; Lan, L.; Liang, H.; Song, X.; Wu, M. *Pseudomonas aeruginosa*: Pathogenesis, virulence factors, antibiotic resistance, interaction with host, technology advances and emerging therapeutics. *Signal Transduct. Target. Ther.* **2022**, *7*, 199. [[CrossRef](#)]
63. Zeng, J.; Platig, J.; Cheng, T.-Y.; Ahmed, S.; Skaf, Y.; Potluri, L.-P.; Schwartz, D.; Steen, H.; Moody, D.B.; Husson, R.N. Protein kinases PknA and PknB independently and coordinately regulate essential *Mycobacterium tuberculosis* physiologies and antimicrobial susceptibility. *PLoS Pathog.* **2020**, *16*, e1008452. [[CrossRef](#)]
64. Zupetic, J.; Peñaloza, H.F.; Bain, W.; Hulver, M.; Mettus, R.; Jorth, P.; Doi, Y.; Bomberger, J.; Pilewski, J.; Nourai, M.; et al. Elastase Activity from *Pseudomonas aeruginosa* Respiratory Isolates and ICU Mortality. *Chest* **2021**, *160*, 1624–1633. [[CrossRef](#)] [[PubMed](#)]
65. Chadha, J.; Harjai, K.; Chhibber, S. Revisiting the virulence hallmarks of *Pseudomonas aeruginosa*: A chronicle through the perspective of quorum sensing. *Environ. Microbiol.* **2022**, *24*, 2630–2656. [[CrossRef](#)] [[PubMed](#)]
66. Bonifacius, A.; Goldmann, O.; Floess, S.; Holtfreter, S.; Robert, P.A.; Nordengrün, M.; Kruse, F.; Lochner, M.; Falk, C.S.; Schmitz, I.; et al. *Staphylococcus aureus* Alpha-Toxin Limits Type 1 While Fostering Type 3 Immune Responses. *Front. Immunol.* **2020**, *11*, 1579. [[CrossRef](#)]
67. Ramstad, S.N.; Wasteson, Y.; Lindstedt, B.-A.; Taxt, A.M.; Bjørnholt, J.V.; Brandal, L.T.; Bohlin, J. Characterization of Shiga Toxin 2a Encoding Bacteriophages Isolated from High-Virulent O145:H25 Shiga Toxin-Producing *Escherichia coli*. *Front. Microbiol.* **2021**, *12*, 728116. [[CrossRef](#)]
68. Angulo-Pineda, C.; Srirussamee, K.; Palma, P.; Fuenzalida, V.M.; Cartmell, S.H.; Palza, H. Electroactive 3D Printed Scaffolds Based on Percolated Composites of Polycaprolactone with Thermally Reduced Graphene Oxide for Antibacterial and Tissue Engineering Applications. *Nanomaterials* **2020**, *10*, 428. [[CrossRef](#)] [[PubMed](#)]
69. Vidakis, N.; Petousis, M.; Velidakis, E.; Tzounis, L.; Mountakis, N.; Boura, O.; Grammatikos, S.A. Multi-functional polyamide 12 (PA12)/multiwall carbon nanotube 3D printed nanocomposites with enhanced mechanical and electrical properties. *Adv. Compos. Mater* **2022**, *31*, 630–654. [[CrossRef](#)]
70. Gao, Z.; Varela, J.A.; Groc, L.; Lounis, B.; Cognet, L. Toward the suppression of cellular toxicity from single-walled carbon nanotubes. *Biomater. Sci.* **2016**, *4*, 230–244. [[CrossRef](#)]
71. Costa, P.M.; Bourgognon, M.; Wang, J.T.W.; Al-Jamal, K.T. Functionalised carbon nanotubes: From intracellular uptake and cell-related toxicity to systemic brain delivery. *J. Control. Release* **2016**, *241*, 200–219. [[CrossRef](#)]
72. Tian, W.; Chen, C.; Lei, X.; Zhao, J.; Liang, J. CASTp 3.0: Computed atlas of surface topography of proteins. *Nucleic Acids Res.* **2018**, *46*, W363–W367. [[CrossRef](#)]
73. Baek, K.; Shin, H.; Cho, M. Multiscale modeling of mechanical behaviors of Nano-SiC/epoxy nanocomposites with modified interphase model: Effect of nanoparticle clustering. *Compos. Sci. Technol.* **2021**, *203*, 108572. [[CrossRef](#)]
74. Trott, O.; Olson, A.J. AutoDock Vina: Improving the speed and accuracy of docking with a new scoring function, efficient optimization, and multithreading. *J. Comput. Chem.* **2010**, *31*, 455–461. [[CrossRef](#)] [[PubMed](#)]
75. Lopéz-Blanco, J.R.; Garzón, J.I.; Chacón, P. iMod: Multipurpose normal mode analysis in internal coordinates. *Bioinformatics* **2011**, *27*, 2843–2850. [[CrossRef](#)]
76. Kovacs, J.A.; Chacón, P.; Abagyan, R. Predictions of protein flexibility: First-order measures. *Proteins* **2004**, *56*, 661–668. [[CrossRef](#)]
77. Ghosh, P.; Bhakta, S.; Bhattacharya, M.; Sharma, A.R.; Sharma, G.; Lee, S.-S.; Chakraborty, C. A Novel Multi-Epitopic Peptide Vaccine Candidate against *Helicobacter pylori*: In-Silico Identification, Design, Cloning and Validation through Molecular Dynamics. *Int. J. Pept. Res. Ther.* **2021**, *27*, 1149–1166. [[CrossRef](#)] [[PubMed](#)]
78. Suhre, K.; Sanejouand, Y.-H. ElNémo: A normal mode web server for protein movement analysis and the generation of templates for molecular replacement. *Nucleic Acids Res.* **2004**, *32*, W610–W614. [[CrossRef](#)] [[PubMed](#)]

Disclaimer/Publisher’s Note: The statements, opinions and data contained in all publications are solely those of the individual author(s) and contributor(s) and not of MDPI and/or the editor(s). MDPI and/or the editor(s) disclaim responsibility for any injury to people or property resulting from any ideas, methods, instructions or products referred to in the content.